AIP | Journal of Applied Physics

Pulsed laser deposited Y 3 Fe 5 O 12 films: Nature of magnetic anisotropy II

S. A. Manuilov and A. M. Grishin

Citation: Journal of Applied Physics **108**, 013902 (2010); doi: 10.1063/1.3446840
View online: http://dx.doi.org/10.1063/1.3446840
View Table of Contents: http://scitation.aip.org/content/aip/journal/jap/108/1?ver=pdfcov
Published by the AIP Publishing

Pulsed laser deposited $Y_3Fe_5O_{12}$ films: Nature of magnetic anisotropy II

S. A. Manuilov and A. M. Grishin[a)]
Department of Condensed Matter Physics, Royal Institute of Technology, SE-164 40 Stockholm-Kista, Sweden

(Received 12 February 2010; accepted 11 May 2010; published online 2 July 2010)

Recently we found epitaxial Fe-deficient yttrium iron garnet $Y_3Fe_{5-t}O_{12-3t/2}$ (YIG) films pulsed laser deposited onto the (111) and (001) face of $Gd_3Ga_5O_{12}$ single crystal experience, respectively, strong rhombohedral and tetragonal distortions and possess unusual magnetic anisotropy. Using the crystal field theory, we explained these anomalies and showed in YIG(111) films ferric ion vacancies preferentially occupy octahedral complexes, order themselves along the [111] growth direction, cause rhombohedral lattice distortions, generate strong uniaxial and significantly reduce cubic crystalline anisotropy, Manuilov *et al.*, [J. Appl. Phys. **106**, 123917 (2009)]. Oxygen vacancies govern electrical neutrality and in spite of high concentration (in access of 7 at. %) they are perfectly ordered that is indicated by narrow ferromagnetic resonance linewidth. The present paper aims to compare growth anisotropies induced in (111) and (001) epitaxial Fe-deficient YIG films. Ordering of vacancies appeared to be different in (111) and (001) oriented YIG films. In highly Fe-deficient YIG(001) we found much smaller imbalance in redistribution of vacancies between the octa- and tetrahedral magnetic sublattices. This feature together with a weaker crystal field in tetrahedral $Fe^{3+}-O^{2-}$ complexes result in reduced growth induced magnetic anisotropy in (001) oriented tetragonal distorted YIGs compared to rhombohedral distorted YIG(111) films. © *2010 American Institute of Physics*. [doi:10.1063/1.3446840]

I. INTRODUCTION

Iron garnet films grown by rf-sputtering[1,2] and pulsed laser deposition technique (PLD) (Refs. 3 and 4) demonstrate properties comparable to films sintered by liquid phase epitaxy (LPE) and being fabricated at much lower temperatures promise solid integration with semiconductor platforms.[5] In laser plasma, due to a high kinetic energy of ablated species, film growth occurs at a very fast rate far away from the thermodynamic equilibrium. This enables synthesis of unique garnet compositions, like $Bi_3Fe_5O_{12}$ (Ref. 6) and $La_3Ga_5O_{12}$,[7] that do not exist in the bulk form because of the violation of the tolerance condition for cation-to-anion radii ratio. Compared to LPE-growth, PLD and rf-magnetron sputtering multisource processing techniques in addition to substitution variability allow garnet properties to be easily tailored by multilayer engineering and continuous solid alloying.

It was found that YIG films PLD-grown at low oxygen pressure show high uniaxial anisotropy and low microwave loss indicated by narrow ferromagnetic resonance (FMR) linewidth.[3] Recently we showed the deficit of Fe ions is responsible for this effect[8] and gave profound explanation for growth induced anisotropy based on single ion molecular field theory.[9] Namely, epitaxial Fe-deficient YIGs PLD-grown onto the (111) and (001) $Gd_3Ga_5O_{12}$ (GGG) substrate experience, respectively, 1.3% rhombohedral and 1.9% tetragonal distortions.[8] Although in both cases supposedly cubic lattice unit cell was stretched along the growth direction, respectively, [111] and [001], films magnetic anisotropy appears to be very different. Fe-deficient YIG(111) yields very strong axial field $H_u=-880$ Oe meanwhile YIG(001), in spite of stronger distortions, showed five times smaller $H_u=-170$ Oe. Later, using FMR spectroscopy we found that unusually high uniaxial anisotropy in PLD-sintered Fe-deficient YIG(111) is accompanied with fivefold reduction in cubic component of magnetocrystalline anisotropy compared to standard LPE-grown YIG. We proved in YIG(111) Fe vacancies preferentially occupy octahedrally coordinated sites with distortion axis perpendicular to the film plane. For octahedral complexes with distortion axes tilted by 19° to the film surface, the probability to remain ferric ion sites vacant is about five times smaller.

Present paper adds physics on the magnetic anisotropy in PLD-grown YIG(001) films. Compared to YIG(111), deficit of Fe^{3+} ions leads to stronger tetragonal type lattice distortions, weaker axial field, and smaller reduction in cubic anisotropy. Similar to YIG(111) films, in (001) YIGs vacancies preferentially occupy octahedral sites though the octa-to-tetra level population ratio varies differently with the concentration of vacancies. For highly Fe-deficient YIGs this ratio being equal to 5.8/1.9, respectively, in (111)/(001) films decreases/increases to 1.5/4.3 value for YIGs with the concentration of Fe vacancies as low as 0.3 f.u. In both types of garnets, "deformation blockage" leads to strong ordering of vacancies within $Fe^{3+}-O^{2-}$ complexes with the distortion axis along the growth direction. The corresponding probability is 0.81 and 0.67 in (001) and (111) films, respectively. However, much higher imbalanced redistribution of vacancies between octa- and tetrahedral sublattices and 1.5 times stronger crystal field is a reason of higher uniaxial anisotropy in highly Fe-deficient (111) oriented YIGs compared to YIG(001) films.

a)Electronic mail: grishin@kth.se

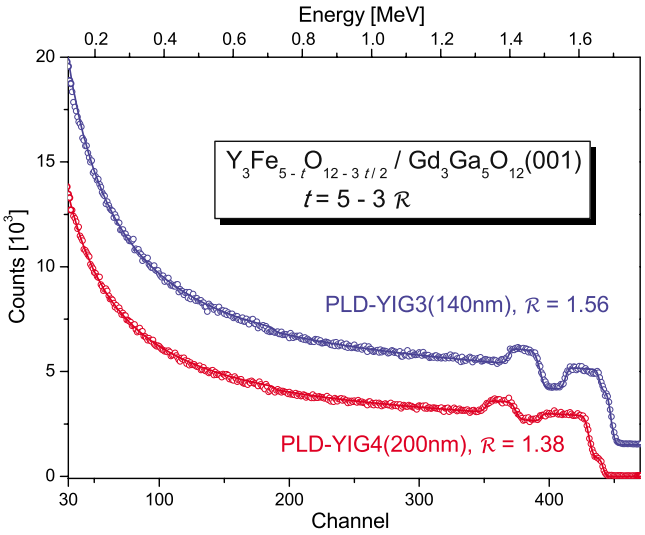

FIG. 1. (Color online) RBS of two YIG films PLD-grown onto $Gd_3Ga_5O_{12}(001)$ single crystal. Symbols are the experimental spectra and solid lines are the simulation made with the SIMNRA 6.05 program. Film thickness and Fe-to-Y concentration ratio $\mathcal{R}$ are shown together with the corresponding sample shorthand. Spectrum of PLD-YIG3 film is offset for clarity by 1500 counts.

Hereinafter, referring to YIG(111) results, we add the roman numeral I to the equations and figures number from our previously published paper.[9]

II. EXPERIMENTAL

The details of PLD-growth of epitaxial YIG films on GGG substrates have been published elsewhere.[8] In brief, YIG targets were ablated by a *Compex-102* KrF 248 nm excimer laser. At 25 mTorr oxygen pressure, GGG substrate temperature of 750 °C, laser energy density of 3–4 J/cm^2, 20 Hz repetition rate, and substrate-to-target distance of 6 cm, the YIG deposition rate was found to be 0.25 Å/shot. Films were *in situ* postannealed at 750 °C and 500 Torr of oxygen pressure for 10 min and slowly cooled down.

We investigated two different types of yttrium iron garnet films grown onto the GGG(001) substrate. Sample PLD-YIG3 was sintered, similar to PLD-YIG1,[9] from the over stoichiometric $Y_2O_3+2\times Fe_2O_3$ oxide target and by x-ray diffraction has been verified to have a cubic structure with a regular, as in YIG single crystal, lattice parameter $a_{YIG}=12.376$ Å.[8] PLD-YIG4 film was grown from the stoichiometric ceramic $Y_3Fe_5O_{12}$ target. Positions of (004) and (008) Bragg reflections fitted with the Nelson–Riley function yield enormously large interplane distance $d_{001}=12.613$ Å. Under assumption of good film-to-substrate in-plane matching, it stands to reason that PLD-YIG4 film experiences strong tetragonal distortions indicated by strong expansion of out-of-film plane YIG lattice parameter compared to GGG substrate: $d_{001}/a_{GGG}-1\approx 1.9\%$.[8]

The stoichiometry of grown films was revealed by Rutherford backscattering spectroscopy (RBS). The measurements were performed using 2.0 MeV $^4He^{2+}$ ion beam that incidents at 0° and the scattering angle was 170°. Symbols in Fig. 1 show experimental RBS spectra recorded for two PLD-YIG samples. Almost 60% difference of Y and Fe atom masses enables accurate determination of the Fe-to-Y concentration ratio $\mathcal{R}$. It was determined fitting experimental data with the SIMNRA 6.05 software.[10] SIMNRA-computed curves are shown in Fig. 1 with solid lines. In PLD-YIG3 film $\mathcal{R}$ was found to be 1.56 that is rather close to the ideal $Y_3Fe_5O_{12}$ stoichiometry with $\mathcal{R}=1.666$. Sample PLD-YIG4 showed anomalously low ratio $\mathcal{R}=1.38$. The relative films thickness measured by the profilometer was in reasonable agreement with the one extracted from the RBS analysis.

As was found previously, epitaxial films grown from the Y-over stoichiometric oxide targets show the same crystalline distortions as the ones deposited from stoichiometrical $Y_3Fe_5O_{12}$ ceramics.[8] The only difference was a widen FMR linewidth. We hereby concluded garnet-type Y stoichiometry is always preserved in PLD-process. Also, very narrow FMR linewidths evidence for the absence of a noticeable amount of ferrous Fe^{2+} ions. Therefore, YIG films composition we define as

$$Y^{3+}{}_3Fe^{3+}{}_{5-t}O^{2-}{}_{12-3t/2}.$$

Here, parameter $t=5-3\mathcal{R}$ is a concentration of ferric Fe^{3+} ion vacancies measured in formula units meanwhile $3t/2$ oxygen O^{2-} vacancies control a charge balance. As shown in Table I, the concentration of Fe^{3+} ions equals $t=0.32$ and 0.86 in PLD-YIG3 and PLD-YIG4 films, correspondingly.

Magnetic anisotropy in PLD-YIGs was explored with the method of FMR. We used our home-built broad band FMR spectrometer[11] to record resonance condition ω_{res} versus H and angular dependence of the resonance field H_{res}. Then these experimental data were fitted using MATLAB program that rigorously accounts orientation of the magnetization $\boldsymbol{M}$ at arbitrarily oriented external magnetic field $\boldsymbol{H}$.

TABLE I. Parameters of PLD-grown Fe-deficient $Y_3[Fe_{2-x}](Fe_{3-y})O_{12-3(x+y)/2}(001)$ films.

		Vacancies distribution			FMR @ $\omega/2\pi=3.5-20$ GHz in geometries $\boldsymbol{H}\perp$ and $\parallel$ to (001)					FMR @ $\omega/2\pi=9.12$ GHz ϕ scan, $\theta_H=0°$			
Sample	Fe-to-Y ratio $\mathcal{R}$	Octa x	Tetra y	$4\pi M_s$ (Gs)	$g_\perp$	$g_\parallel$	H_u^* (Oe)	K_u (10^4 erg/cm^3)	H_c (Oe)	H_u^* (Oe)	K_u (10^4 erg/cm^3)	H_c (Oe)	K_1 (10^3 erg/cm^3)
PLD-YIG3 (140 nm)	1.56	0.26	0.06	1834	1.998 ±0.003	2.004 ±0.012	−1987 ± 41	−1.12	−44 ± 31	−2029 ± 47	−1.42	−57 ± 3	−4.17
PLD-YIG4 (200 nm)	1.38	0.56	0.30	1498	2.003 ±0.003	2.014 ±0.006	−2160 ± 52	−3.95	−37 ± 46	−2152 ± 30	−3.90	−31 ± 3	−1.84

III. THEORETICAL EXCERPTS

Free energy density in (001) oriented YIG

$$F = -HM_s[\cos\theta_H\cos\theta_M + \sin\theta_H\sin\theta_M\cos(\phi_H-\phi_M)] + K_u^*\sin^2\theta_M + \frac{1}{4}K_1(\sin^2 2\theta_M + \sin^4\theta_M\sin^2 2\phi_M), \quad (1)$$

accounts Zeeman energy (the first term) and energies of uniaxial and cubic crystalline magnetic anisotropy defined, respectively, by the effective constant $K_u^*=K_u-2\pi M_s^2$ and K_1. Here M_s is a saturation magnetization, polar θ and azimuth ϕ angles with the corresponding subscripts M and H set the orientation of $\boldsymbol{M}$ and $\boldsymbol{H}$ vectors (see below inset to Fig. 3). In bulk $Y_3Fe_5O_{12}$ single crystal, K_1 is negative that makes cube body diagonal direction [111] to be magnetic "easy" axis, face diagonal [110] to be a "medium" axis, and a "hard" axis is parallel to the cubic edge direction [100].

The equilibrium orientation of the magnetization vector $\boldsymbol{M}(\boldsymbol{H})$ must be determined from the condition of the minimum of free energy

$$\frac{\partial F}{\partial\theta_M} \equiv HM_s[\cos\theta_H\sin\theta_M - \sin\theta_H\cos\theta_M\cos(\phi_H-\phi_M)] + \frac{1}{2}H_u^*M_s\sin 2\theta_M + \frac{1}{4}H_cM_s\sin 2\theta_M(2\cos 2\theta_M + \sin^2\theta_M\sin^2 2\phi_M) = 0,$$

$$\frac{\partial F}{\partial\phi_M} \equiv -HM_s\sin\theta_H\sin\theta_M\sin(\phi_H-\phi_M) + \frac{1}{4}H_cM_s\sin^4\theta_M\sin 4\phi_M = 0. \quad (2)$$

Here we introduced the effective fields of uniaxial $H_u^*=2K_u^*/M_s$ and cubic $H_c=2K_1/M_s$ magnetic anisotropy.

In saturated ferromagnet the magnetization experiences precession with the characteristic FMR frequency ω_{res} derived by Suhl and Smit[12]

$$\left(\frac{\omega_{res}}{\gamma}\right)^2 = \frac{1}{M_s^2\sin^2\theta_M}\left[\frac{\partial^2F}{\partial\theta_M^2}\frac{\partial^2F}{\partial\phi_M^2} - \left(\frac{\partial^2F}{\partial\theta_M\partial\phi_M}\right)^2\right]. \quad (3)$$

Here $\gamma=g\mu_B/\hbar$ is the gyromagnetic ratio expressed through the g-factor, Bohr magneton μ_B, and Planck constant $\hbar$. Differentiating free energy F from Eq. (1) two times and using the equilibrium conditions from Eq. (2) we present the expression for FMR frequency as follows:

$$\left(\frac{\omega_{res}}{\gamma H}\right)^2 = \left[\frac{\cos\theta_H}{\cos\theta_M} + \frac{H_u^*}{H} + \frac{H_c}{H}\times\left(\cos^2\theta_M - \frac{3}{2}\sin^2\theta_M\sin^2 2\phi_M\right)\right]\times\left\{\cos\theta_H\cos\theta_M + \sin\theta_H\sin\theta_M\cos(\phi_H-\phi_M) + \frac{H_u^*}{H}\cos 2\theta_M + \frac{H_c}{H}\left[\cos 4\theta_M + \frac{1}{4}\sin^2 2\phi_M(\cos 2\theta_M - \cos 4\theta_M)\right]\right\} - \left(\frac{3H_c}{4H}\right)^2\sin^4\theta_M\cos^2\theta_M\sin^2 4\phi_M. \quad (4)$$

Complete set of Eqs. (2) and (4) indirectly defines FMR relation ω versus H (or vice versa) at various orientations of magnetic field. Worthy of note, FMR in Ca, Co, and Ge doped LPE-grown (111), (001), and (110) YIG films has been studied by Maryško and Šimšová taking into account uniaxial, the first and second order cubic anisotropies.[13]

In three limiting cases Eq. (4) can be reduced to the compact plain formulas.

- In perpendicular magnetic field $\boldsymbol{H}\|[001]$ ($\theta_H=0$) if $H\geq|H_u^*|+|H_c|$, then $\theta_M=0$ and

$$\omega_{res} = \gamma_{[001]}(H - |H_u^*| - |H_c|). \quad (5a)$$

- For in-plane magnetic field $\boldsymbol{H}\|[100]$ ($\theta_H=\pi/2$, $\phi_H=0$) if $H\geq|H_c|$, then $\theta_M=\pi/2$, $\phi_M=0$, and

$$\omega_{res} = \gamma_{[100]}\sqrt{(H+|H_u^*|-|H_c|)(H-|H_c|)}. \quad (5b)$$

- For in-plane magnetic field parallel to the face diagonal $\boldsymbol{H}\|[110]$ ($\theta_H=\pi/2$, $\phi_H=\pi/4$) always $\theta_M=\pi/2$, $\phi_M=\pi/4$, and

$$\omega_{res} = \gamma_{[110]}\sqrt{\left(H+|H_u^*|-\frac{1}{2}|H_c|\right)(H+|H_c|)}. \quad (5c)$$

Equation (5c) can be used also to define FMR frequency at zero magnetic field

$$\omega_{res} = \gamma_{[110]}\sqrt{|H_c|\left(|H_u^*|-\frac{1}{2}|H_c|\right)}. \quad (6)$$

This expression assumes a film is uniformly in-plane magnetized (single domain state) along [110] direction. Accounting shape and magnetocrystalline anisotropy, this is magnetic "easy" axis in YIG(001) film.

IV. FMR SPECTROSCOPY

FMR method provides reliable characteristics of iron garnet films: gyromagnetic g-factor, axial K_u^* and cubic K_1 constants of anisotropy. Raw data for the resonance field H_{res} at given frequency ω are obtained from the position of FMR absorption lines exemplified in Fig. 2. These plots were drawn by numerical integration of the differential FMR absorption $d\chi''/dH$ experimentally recorded with a lock-in detection technique. Here δH defines FMR line full width at half maximum. Both types, Fe-rich and Fe-deficient films, were grown at processing conditions that have been optimized to get the narrowest linewidth δH. In Fe-deficient films δH appeared to be always narrower compared to films sintered from Fe-over stoichiometric oxide target, see Fig. 2.

A. Broadband spectroscopy

Field of uniaxial anisotropy $H_u^*=2K_u^*/M_s$ and g-factor were determined with a high accuracy exciting FMR with the shorted microstrip line. In Fig. 3 we show FMR ω_{res} versus

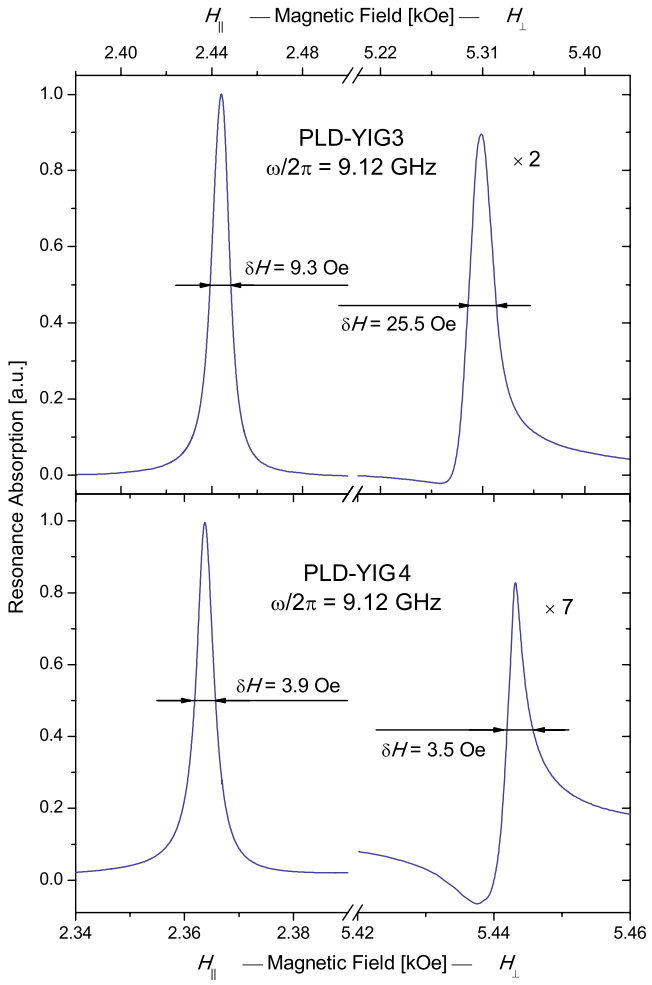

FIG. 2. (Color online) FMR absorption in PLD-YIG3 and PLD-YIG4 films recorded at frequency $\omega/2\pi$=9.12 GHz in magnetic field parallel (left frame) and perpendicular (right frame) to the film plane.

H spectra recorded in broad frequency range 200 MHz to 20 GHz in three different orientations of external magnetic field: perpendicular to the film plane $\boldsymbol{H}\|[001]$ and two in-plane directions $\boldsymbol{H}\|[100]$ and $\boldsymbol{H}\|[110]$ (see the coordinate system in inset to Fig. 3). Solid lines in Fig. 3 are drawn for eye guiding along the symbols that reproduce the experimental data. These lines exactly coincide with $\omega_{res}(H)$ curves computed from the Eqs. (5) in strong magnetic field where the film is uniformly magnetized (see the detailed discussion below). Fitting parameters H_u^*, H_c, and g-factors are collected in Table I in the column "geometries $\boldsymbol{H}$ ⊥ and ∥ to (001)." Within experimental errors g-factor was found to be isotropic and identical in Fe-rich and Fe-deficient films. Effective field H_u^* in Fe-deficient tetragonal distorted PLD-YIG4 film is 9% greater than that in Fe-rich cubic PLD-YIG3.

B. "Soft" modes

In perpendicular magnetic field $\boldsymbol{H}\|[001]$, FMR spectra in Fig. 3 demonstrate occurrence of the "soft mode." As seen from Eq. (5a), FMR frequency ω_{res} goes to zero in magnetic field $H_0=|H_u^*|+|H_c|$. At this field uniformly perpendicular magnetized state $\boldsymbol{M}\|[001]$ becomes unstable regarding the nucleation of magnetic domains with in-plane components of

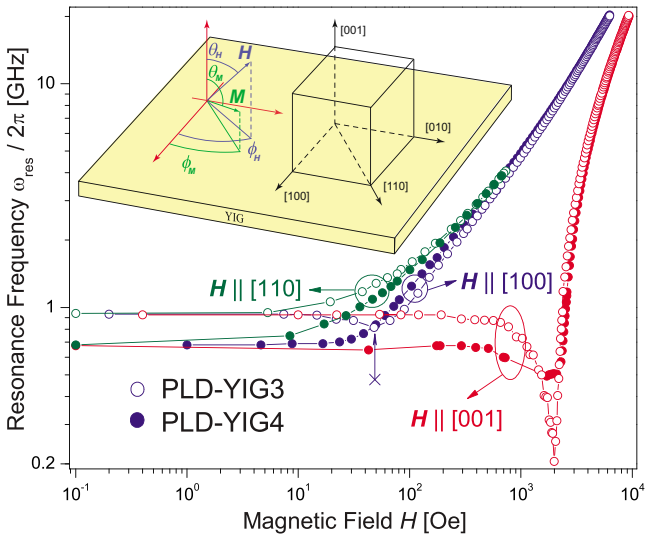

FIG. 3. (Color online) Dependencies of FMR frequency ω_{res} on the external magnetic field $\boldsymbol{H}$ in perpendicular $\boldsymbol{H}\|[001]$ and two parallel to the film plane geometries: $\boldsymbol{H}\|[110]$ and $\boldsymbol{H}\|[100]$. PLD-YIG3 and PLD-YIG4 films spectra are shown with symbols ○ and ●, correspondingly. Solid lines depict the fitting of the experimental data to analytical formulas [Eqs. (5a)–(5c) and (6)]. The fitting parameters $g=\gamma\hbar/\mu_B$, H_u^*, and H_c are collected in Table I. Inset presents the coordinate system of (001) oriented YIG film. Deep cove at 2000 Oe and indistinct pit at 48 Oe marked with a crossed vertical arrow manifest presence of spin wave "soft modes."

magnetization $\boldsymbol{M}$ oriented along one of the equivalent [110], $[\bar{1}10]$, $[\bar{1}\bar{1}0]$, and $[1\bar{1}0]$ directions. This reorientation phase transition can be detected at very low, even audio, frequencies as anomalous increase in magnetic susceptibility.

For in-plane magnetic field, uniform magnetization (single domain state) is realized at $H \gg |H_c|$ where experimental data, shown with symbols in Fig. 3, are nicely fitted to $\omega_{res}(H)$ dependencies from Eqs. (5b) and (5c). Equation (5b) predicts also existence of another "soft mode" if magnetic field is oriented along the "hard" in-plane magnetization direction $\boldsymbol{H}\|[100]$. When decreasing magnetic field reaches $H_0=|H_c|$, the uniformly magnetized state decomposes into domains with nonzero projections of the magnetization $\boldsymbol{M}$ on to the [010] and $[0\bar{1}0]$ axes. This mode manifests itself by indistinct minimum at the ω_{res} versus H spectrum of PLD-YIG3 film which we marked with crossed vertical arrow in Fig. 3.

Asymptotic formula in Eq. (6) for ω_{res} at $H \to 0$ and the reorientation fields $H_0=|H_u^*|+|H_c|$ and $H_0=|H_c|$, respectively, in perpendicular and in-plane geometries may serve as independent methods to determine fields of magnetic anisotropy. These calculations yield the values of H_u^* and H_c that are close to those that were obtained fitting the broad band FMR spectra in Fig. 3 (see Table I).

C. Angular resolved FMR

As an additional check, in Fig. 4 we compared experimentally recorded and simulated with Eqs. (2) and (4) polar angle dependencies of the resonance field $H_{res}(\theta)$ at $\omega/2\pi$ =9.12 GHz and $\boldsymbol{H}\|(100)$. Within experimental accuracy the same parameters H_u^* and H_c provide a good matching of measured and computed data.

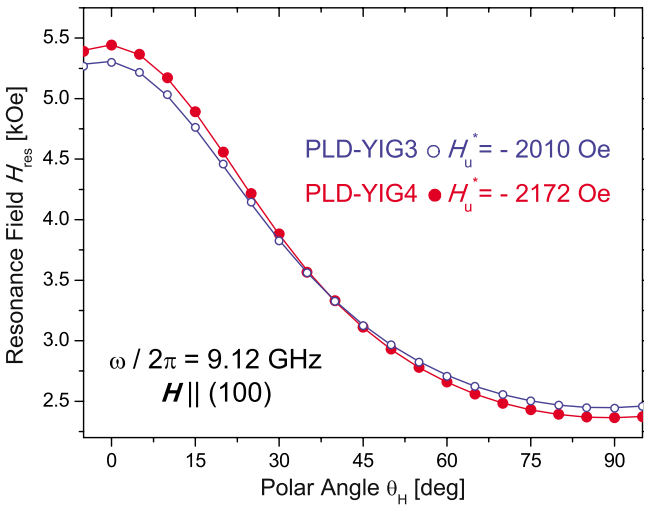

FIG. 4. (Color online) Polar angle dependence of the resonance field $H_{res}(\theta_H, \phi=0)$ recorded at $\omega/2\pi=9.12$ GHz. Experimental data for PLD-YIG3 and PLD-YIG4 films are shown with symbols ○ and ●, correspondingly. Solid lines are theoretical curves computed with Eqs. (4) and (2) using axial H_u^* and cubic H_c fields as fitting parameters.

General expression for FMR frequency in Eq. (4) always contains small field of cubic anisotropy H_c in combination with a large H_u^*. Their big difference significantly reduces an accuracy of the determination of H_c and leads to big fitting errors in all the above-mentioned experiments performed at special orientations of magnetic field. To infer reliable parameters of cubic field H_c statistical sampling of experimental data must be acquired. The measurements of the in-plane angular dependence of the resonance field $H_{res}(\theta_H = \pi/2, \phi_H)$ provide demanded accuracy.

These experiments were carried out in rectangular microwave cavity at frequency $\omega/2\pi=9.12$ GHz (TE_{106} mode) rotating magnetic field in (001) film-plane (in inset to Fig. 3 $\theta_H=\pi/2$ and azimuth angle ϕ_H is varied). In this geometry, the resonance field $H_{res}(\phi)$ experiences the maximum variation that additionally raises the accuracy of the determination of cubic anisotropy. Experimental $H_{res}(\phi)$ dependencies are shown with symbols in Fig. 5. They clearly demonstrate 90° periodicity since the rotational direction [001] is a fourfold symmetry axis. To eliminate the artifacts caused by inaccurate sample positioning we performed Fourier transformation of experimental angular dependence

$$H_{res}(\phi) = A_0 + \sum_{n=1}^{\infty} \{A_n \cos[n(\phi_H + \phi_0)] + B_n \sin[n(\phi_H + \phi_0)]\}, \quad (7)$$

and show Fourier harmonics in insets to Fig. 5. Here $\phi_0 = \phi_H - \phi$ is an unintentional shift of experimental azimuth ϕ angle.

The zeroth harmonic A_0 equals to the average value of $H_{res}(\phi)$ and determines field of uniaxial anisotropy $H_u^*=-2029$ Oe and -2152 Oe for PLD-YIG3 and PLD-YIG4, correspondingly. These values within 1.5% accuracy coincide with H_u^* determined from the broadband measurements in Fig. 3. The fourth Fourier harmonic is related to cubic anisotropy. Results of theoretical modeling based on Eqs. (4) and (2) fit experimental fourth Fourier amplitudes with $H_c=-57$ Oe and -31 Oe, respectively, for PLD-YIG3 and PLD-YIG4 films. As seen in Table I, these parameters are valid within 10% of accuracy.

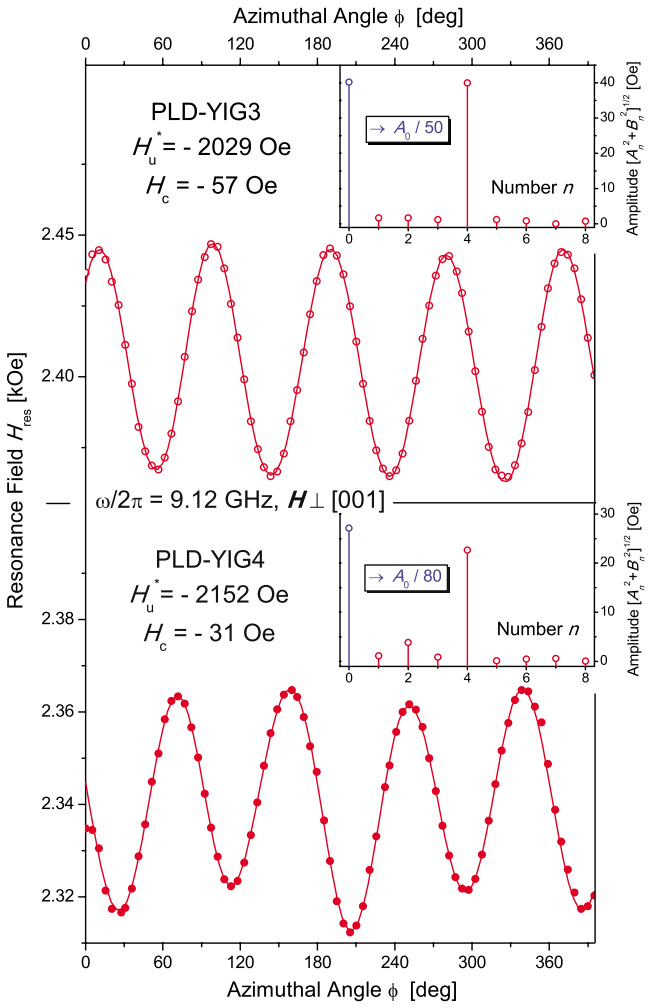

FIG. 5. (Color online) In-plane angular dependence of the resonance field $H_{res}(\theta_H=\pi/2, \phi)$ recorded at $\omega/2\pi=9.12$ GHz. Symbols ○ and ● depict experimental data for PLD-YIG3 and PLD-YIG4 films, respectively. Solid lines present fitting to the Fourier series in Eq. (7). The eight beginning Fourier amplitudes are shown in insets. Fitting parameters, axial H_u^*, and cubic H_c fields, are printed together with the corresponding sample shorthand.

V. CRYSTAL FIELD THEORY

In this chapter, to explain observed effects of magnetic anisotropy we will employ crystal field theory to earlier introduced "Fe vacancy model."[9] It is based on two assumptions. The first, Fe^{3+} vacancies are grouped together with the compensating O^{2-} vacancies that provide a charge balance. The second, ferric ion vacancy behaves similar to a diamagnetic cation substituent changing net magnetization and single ion crystal field anisotropy.

A. Concentration dependence of magnetization

We start with the saturation magnetization in Fe-deficient YIGs

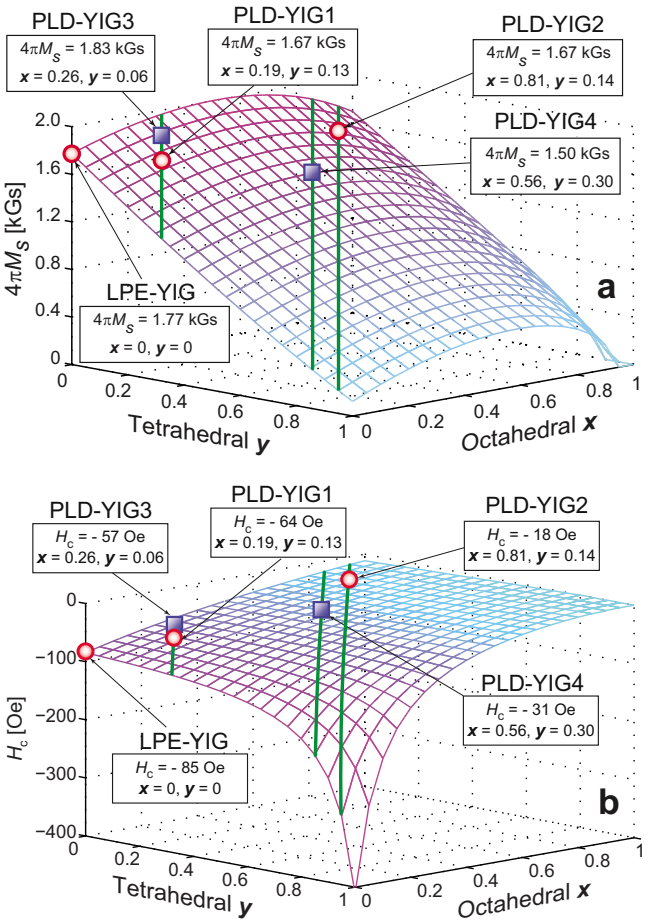

FIG. 6. (Color online) 3D contour plots for concentration dependence of saturation magnetization $4\pi M_s$ (a) and cubic anisotropy field H_c (b) in Fe-deficient $\{Y_3\}[Fe_{2-x}](Fe_{3-y})O_{12-3(x+y)/2}$ films. Three solid lines depict variation in $4\pi M_s$ and H_c in YIGs when the total concentration of Fe ions is kept constant $t=x+y=0.32$, 0.86, and 0.95 f.u. whereas the partial concentrations in octahedral x and tetrahedral sublattice y vary. Three circular symbols mark $4\pi M_s$ and H_c in (111) oriented LPE-YIG, PLD-YIG1, and PLD-YIG2 films from Ref. 9. Big quadratic symbols show experimental H_c and calculated $4\pi M_s$ parameters for PLD-YIG3 and PLD-YIG4 films grown onto GGG(001) crystal. Symbols projections to the (x,y) plane yield actual redistribution of Fe ions between octahedral x and tetrahedral y sublattices.

$$\{Y_3\}[Fe_{2-x}](Fe_{3-y})O_{12-3(x+y)/2}.$$

Here x and y denote the numbers of Fe^{3+} vacancies per formula unit that occupy, respectively, $8x$ of 16 octahedral $[a]$ and $8y$ of 24 tetrahedral (d) garnet crystal sites. Saturation magnetization $4\pi M_s$ at different concentrations of x octahedral and y tetrahedral Fe vacancies has been calculated in Ref. 9 from the complete set of equations Eqs. (I.9–12). These equations present Weiss molecular field theory added with empirical Geller–Dionne corrections to the magnetic moments in $[a]$ and (d) magnetic sublattices[14,15] and Dionne's intra- and inter-sublattice molecular field coefficients.[15]

In Fig. 6(a) three-dimensional (3D) contour $4\pi M_s(x,y)$ plot shows the dependence of the net saturation magnetization (the sum of octahedral and tetrahedral contributions) on the levels of x and y of Fe^{3+} vacancies. Three solid lines depict $4\pi M_s$ in YIGs with the total concentration of Fe vacancies $t=x+y$ equals to 0.32, 0.86, and 0.95 f.u. Herewith big circular symbols and shorthands present calculated values of $4\pi M_s$ obtained in Ref. 9 (see Fig. I.6a) for the reference LPE-YIG, PLD-YIG1, and PLD-YIG2 (111) oriented films. The actual computed value of $4\pi M_s$ in two PLD-YIG(001) films will be added and marked on these lines with quadratic symbols as soon as partial concentrations x and y will be determined.

B. Concentration dependence of cubic anisotropy

To find the redistribution of Fe vacancies between octahedral and tetrahedral magnetic sublattices we compared experimentally measured and theoretically calculated fields of cubic anisotropy H_c. Anisotropy energy K_1 and cubic field $H_c=2K_1/M_s$ have been calculated in Ref. 9 using complete set of equations Eqs. (I.9–14) and (I.18). In Fig. 6(b)) the computed 3D contour plot presents cubic field $H_c(x,y)$ for different distribution of ferric vacancies between $[a]$ and (d) sublattices. Similar to Fig. 6(a)), three solid lines on the contour surface show how theoretical value H_c varies when the total concentration is kept constant $t=x+y=0.32$, 0.86, and 0.95 f.u. whereas both x and y vary.

To determine actual concentration of vacancies x in $[a]$ and y in (d) sublattices, we set experimentally measured values $H_c=-57$ Oe for PLD-YIG3 and $H_c=-31$ Oe for PLD-YIG4 film on to the contour surface and the corresponding lines $t=0.32$ and 0.86. These experimental points are shown with big quadratic symbols in Fig. 6(b). Projecting the positions of the quadratic symbols onto the (x,y) plane we obtain $x=0.28$, $y=0.04$ for PLD-YIG3 and $x=0.56$, $y=0.30$ for PLD-YIG4 (see Table I). Having determined the partial concentrations x and y, we came back to Fig. 6(a) and marked there the corresponding computed values of $4\pi M_s$ with quadratic symbols.

For completeness, in Fig. 6(b) with big circular symbols and shorthands we also present experimental H_c values for LPE-YIG, PLD-YIG1, and PLD-YIG2 (111) films obtained in Ref. 9 and shown there in Fig. I.6b.

Comparing (111) and (001) PLD-grown YIGs we can make the following conclusions. For both orientations of YIG films copious amount of Fe vacancies populate octahedral sites, i.e., $x>y$. Preferential occupation of vacancies in octahedral sublattice in YIG(111) films is much stronger at high and negligible at low concentration of vacancies t unlike YIG(001) garnets where it is prominent at low and significantly decreases at high concentration t. Strong dilution of tetrahedral sublattice by abundant amount of ferric vacancies in YIG(001) films leads to noticeable reduction in saturation magnetization $4\pi M_s$.

C. Uniaxial anisotropy

Now, knowing the redistribution of vacancies between octahedral x and tetrahedral y magnetic sublattices, we can utilize experimental data for effective field H_u^* to define which $Fe^{3+}-O^{2-}$ complexes belonging to the same magnetic sublattice are preferentially occupied by Fe vacancies. This procedure will be performed in the following sequence. Experimental $H_u^*(x,y)$ and calculated $4\pi M_s(x,y)$ values will be used to determine uniaxial anisotropy energy

TABLE II. Ferric ion sites in the garnet structure of YIG(001) film.

Octahedral [a] cites		
Number of cites	Distortion $\boldsymbol{\alpha}$ axis	Directional cosines of $\boldsymbol{\alpha}$ axis
4	[111]	$1/\sqrt{3},\ 1/\sqrt{3},\ 1/\sqrt{3}$
4	$[\bar{1}\bar{1}1]$	$-1/\sqrt{3},\ -1/\sqrt{3},\ 1/\sqrt{3}$
4	$[1\bar{1}\bar{1}]$	$1/\sqrt{3},\ -1/\sqrt{3},\ -1/\sqrt{3}$
4	$[\bar{1}1\bar{1}]$	$-1/\sqrt{3},\ 1/\sqrt{3},\ -1/\sqrt{3}$

Tetrahedral [d] cites			
Group number	Number of cites	Distortion $\boldsymbol{\alpha}$ axis	Directional cosines of $\boldsymbol{\alpha}$ axis
First	8	[001]	0, 0, 1
Second	8	[010]	0, 1, 0
	8	[100]	1, 0, 0

$$K_u = \frac{M_s}{2}(H_u^* + 4\pi M_s). \tag{8}$$

Then, following Wolf,[16] we will calculate anisotropic part of the free energy using Eqs. (I-19) and (I-20) that summarize anisotropies from all Fe^{3+} ions on $16\times(1-x/2)$ octahedral [a] and $24\times(1-y/3)$ tetrahedral (d) sites and then will compare computed value with Eq. (8).

Classification of all Fe ions sites in the garnet structure of YIG(001) films is presented in Table II with the directions $\boldsymbol{\alpha}$ of the local distortion axes and their directional cosines (see also Refs. 17 and 18). In octahedral sublattice all 16 sites for the (001) growth face are equivalent. Calculation of the scalar product $(\boldsymbol{M}\boldsymbol{\alpha}_i)^2$ in Eq. (I.19) with the directional cosines shown in Table II and averaging it over $i_{\max}=16\times(1-x/2)$ [a] sites gives $\Sigma_i((\boldsymbol{M}\boldsymbol{\alpha}_i)^2/M_s^2)\equiv(16/3)\times(1-x/2)$. This is an additive constant to the free energy that does not depend on the vector $\boldsymbol{M}$ direction thus does not contribute to the anisotropy.

In tetrahedral sublattice there are two nonequivalent Fe ion positions: eight sites from the first group with the out-off growth plane distortion axis [001] and 16 sites from the second group with the distortion axes parallel to the film plane (001). Averaging their contributions over $i_{\max}=24\times(1-y/3)(d)$ sites gives us

$$\sum_i \frac{(\mathbf{M}\boldsymbol{\alpha}_i)^2}{M_s^2}\kappa_i \equiv 8\kappa_1 \cos^2\theta_M + 8\kappa_2 \sin^2\theta_M. \tag{9}$$

Here θ_M is the polar angle that defines the direction of the vector $\boldsymbol{M}$ in spherical coordinate system shown in inset to Fig. 3. Equation (9) takes into account that nonequivalent eight tetrahedral sites from the first and 16 tetrahedral sites from the second group (see Table II) might be populated with unequal probabilities κ_1 and κ_2. As a result, the angular dependent part of the free energy from Eq. (I.19) that describes uniaxial anisotropy takes the form

$$\delta F \equiv K_u \sin^2\theta_M = -8D_d p_d(\kappa_1-\kappa_2)\sin^2\theta_M. \tag{10}$$

The last stage in the calculation of K_u is to determine the population difference $(\kappa_1-\kappa_2)$ using the preferential site ordering model suggested by Callen.[19] Similar to what has been done in Ref. 9 for octahedral sites, now we introduce for *tetrahedral* sites two "sticking coefficients" κ_1^o and κ_2^o. They define the fractions of tetrahedral sites, respectively, in the first and the second group populated by ferric ions if an equal number of Fe ions and Fe vacancies are available for a lodging: $y=3/2$. Then the population difference will become to equal

$$\kappa_1-\kappa_2 = \frac{(3-y)\kappa_1^o}{y(1-\kappa_1^o)+(3-y)\kappa_1^o} - \frac{(3-y)\kappa_2^o}{y(1-\kappa_2^o)+(3-y)\kappa_2^o}. \tag{11}$$

Finally, substituting Eq. (11) into Eq. (10) the uniaxial anisotropy energy K_u in Fe-deficient YIG(001) films can be expressed in the following form:

$$K_u[\mathrm{erg/cm^3}] = -\frac{2\pi\hbar c}{V}8D_d p_d(T,x,y) \times \frac{y(3-y)(\kappa_1^o-\kappa_2^o)}{\left[y+2\kappa_1^o\left(\frac{3}{2}-y\right)\right]\left[y+2\kappa_2^o\left(\frac{3}{2}-y\right)\right]}. \tag{12}$$

To calculate actual magnitude of noncubic anisotropy, we use the crystal field coefficient $D_d=-0.0885\ \mathrm{cm^{-1}}$ at 295 K obtained by Geschwind[17] from paramagnetic resonance of Fe^{3+} ion in tetrahedral sites in Fe-substituted $Y_3Ga_5O_{12}$ garnet and factor $p_d(x,y)$ calculated using Eqs. (I.10–12) and (I.20). The resultant uniaxial anisotropy energy $K_u[\mathrm{erg/cm^3}]$ in PLD-grown YIG(001) films for different modeling parameters κ_1^o and κ_2^o is shown in Fig. 7.

VI. VACANCIES ORDERING

Both Geschwind's coefficient D_d at 295 K (Ref. 17) and experimentally observed K_u in Table I are negative. This implies $(\kappa_1^o-\kappa_2^o)<0$ that is the higher probability for Fe ions to populate tetrahedral sites from the second group. Correspondingly, Fe^{3+} and accompanying them O^{2-} vacancies preferentially occupy tetrahedral complexes from the first group with the distortion axis along [001] growth direction. To quantify the level of redistribution of vacancies between different complexes of the same tetrahedral sublattice, we compared computed and experimental results for K_u. In Fig. 7 each solid line marks the intersection of theoretical 3D contour $K_u(\kappa_1^o,\kappa_2^o)$ with the plane K_u=const that represents the experimentally measured value of K_u from Table I. To determine the modeling parameters κ_1^o and κ_2^o we make projections of these intersecting lines onto the common (κ_1^o,κ_2^o) plane. Their projections are passing very close to each other. The magnified plot in inset to Fig. 7 reveals they intersect each other nearby the point

$$\kappa_1^o = 0.19,\quad \kappa_2^o = 0.78. \tag{13}$$

These values of sticking coefficients define the population probabilities for ferric ions in the first and the second group of sites in tetrahedral sublattice. Correspondingly, the probability for individual Fe vacancy in YIG(001) films to occupy tetrahedrons with distortion axis parallel to the growth

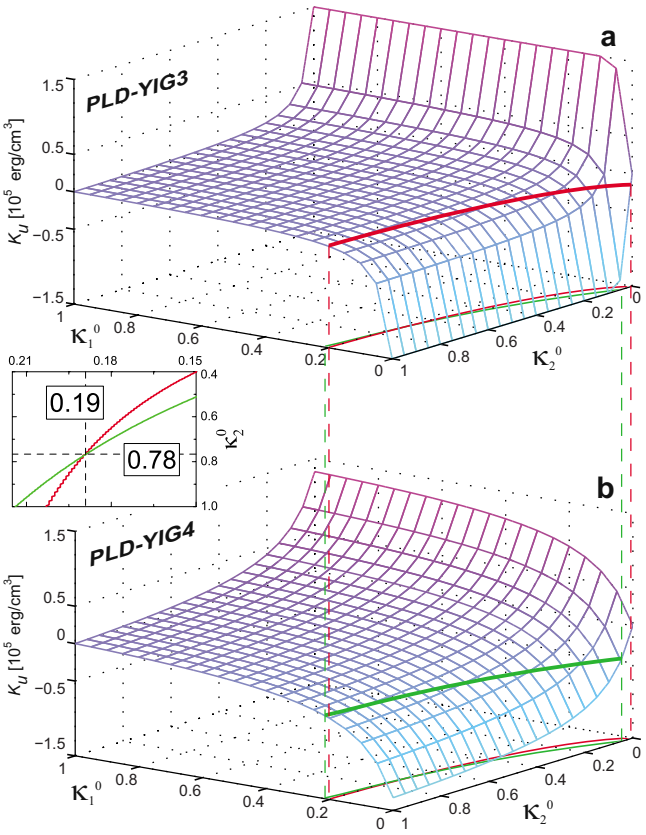

FIG. 7. (Color online) Calculated energy of uniaxial magnetic anisotropy K_u in PLD-YIG(001) films for different "sticking coefficients" κ_1^o and κ_2^o that define the probabilities to populate the first and the second group of the tetrahedral sites with Fe^{3+} ions (see Table II). Solid lines on the contour surfaces show the experimental magnitude of K_u measured in PLD-YIG3 (a) and PLD-YIG4 (b) films. The projections of these two lines onto the (κ_1^o, κ_2^o) plane intersect each other nearby the point $\kappa_1^o=0.19$ and $\kappa_2^o=0.78$. Lucid image of the intersection is magnified in inset. The modeling parameters determine two probabilities: $1-\kappa_1^o=0.81$ and $1-\kappa_2^o=0.22$ for Fe^{3+} vacancy to occupy, respectively, tetrahedrons distorted along the growth [001] direction and tetrahedral complexes with in-plane distortion axes.

[001] direction equals $1-\kappa_1^o=0.81$ compared to $1-\kappa_2^o=0.22$ for the Fe-empty tetrahedral complexes with distortion axes directed along the film surface.

Analogously to YIG(111) garnets, the effect of "deformation blockage" causes the ordering of Fe vacancies in YIG(001) films within $Fe^{3+}-O^{2-}$ complexes that experience tensile distortions along the growth direction. The only difference is the symmetry of Fe-empted sites: octahedral FeO_6 complexes in YIG(111) and tetrahedral FeO_4 ones in YIG(001) films. The complexes which distortion axes parallel to the film plane are much stronger bonded with the substrate and underlayers than those which freely deform along the growth direction. Although the same mechanism is responsible for growth anisotropy, the resultant induced magnetic anisotropy has different magnitude in two growth geometries. In YIG(001) films uniaxial magnetic anisotropy is 70% smaller ($|K_u|=3.90\times10^4$ erg/cm^3 compared to 6.57×10^4 erg/cm^3) whereas the lattice distortions is almost 50% larger ($d_{001}/a_{GGG}-1=1.9\%$ compared to $d_{111}/a_{GGG}\sqrt{3}-1=1.3\%$) than those in YIG(111) films. Much smaller difference in Fe vacancies redistribution between octa- and tetrahedral sites as well as weaker crystal field in tetrahedral complexes ($D_d=-0.0885$ cm^{-1} compared to $D_a=-0.1295$ cm^{-1}, Ref. 17) is a reason for smaller growth induced magnetic anisotropy in highly Fe-deficient YIG(001) films.

VII. CONCLUSIONS

Consistent molecular field theory explains the effects of reduced cubic and strong negative growth induced uniaxial magnetic anisotropy in epitaxial iron deficient yttrium iron garnet films. Suggested "Fe vacancy model" is based on the assumption that ferric ion vacancies behave similar to diamagnetic ions substituted into the octahedral and tetrahedral YIG sublattices. All the features of unusual magnetic anisotropy observed in pulsed laser deposited (111) and (001) oriented YIGs were quantitatively described within single ion molecular field theory using crystal field parameters revealed from the earlier published experiments on diamagnetic ion substituted $Y_3Fe_5O_{12}$ and Fe-substituted isomorphous diamagnetic garnets. As a common for (111) and (001) YIGs feature, ferric ion and charge balancing oxygen vacancies preferentially lodge themselves in octahedral magnetic sublattice. Stronger imbalance in redistribution of vacancies between octa- and tetrahedral sublattices occurs at high/low concentration of vacancies, respectively, in (111)/(001) YIG films. Growth induced uniaxial magnetic anisotropy in Fe-deficient YIGs is caused by the preferential vacancies population of $Fe^{3+}-O^{2-}$ complexes with the distortion axes parallel to the growth direction. Such ordering of vacancies occurs within octahedral FeO_6 and tetrahedral FeO_4 coordinated complexes in YIG(111) and YIG(001) garnets, respectively. Higher relative concentration of tetrahedral vacancies is responsible for stronger lattice distortions whereas weaker crystal field affecting tetrahedral coordinated Fe^{3+} ion is a reason of lower axial field in Fe-deficient YIG(001) compared to YIG(111) garnets.

ACKNOWLEDGMENTS

The authors gratefully acknowledge Dr. S. I. Khartsev for the synthesis of YIG films. This work was partially supported by the Vetenskapsrådet (Swedish Research Council), Swedish Institute, and Science and Innovation Agency of Russian Federation ГК No. 02.740.11.5179.

[1] J.-P. Krumme, V. Doormann, B. Strocka, and P. Willich, J. Appl. Phys. **60**, 2065 (1986).
[2] M. Gomi, H. Furuyama, and M. Abe, J. Appl. Phys. **70**, 7065 (1991).
[3] P. C. Dorsey, S. E. Bushnell, R. G. Seed, and C. Vittoria, J. Appl. Phys. **74**, 1242 (1993).
[4] M. Y. Chern, C. C. Fang, J. S. Liaw, J. G. Lin, and C. Y. Huang, Appl. Phys. Lett. **69**, 854 (1996).
[5] R. Karim, S. A. Oliver, and C. Vittoria, IEEE Trans. Magn. **31**, 3485 (1995); H. Buhay, J. D. Adam, M. R. Daniel, N. J. Doyle, M. C. Driver, G. W. Eldridge, M. H. Hanes, R. L. Messham, and M. M. Sopira, *ibid.* **31**, 3832 (1995); S.-Y. Sung, X.-Y. Qi, and B. J. H. Stadler, Appl. Phys. Lett. **87**, 121111 (2005); Y.-M. Kang, S.-H. Wee, S.-I. Baik, S.-G. Min, S.-C. Yu, S.-H. Moon, Y.-W. Kim, and S.-I. Yoo, J. Appl. Phys. **97**, 10A319 (2005).
[6] N. Adachi, V. P. Denysenkov, S. I. Khartsev, A. M. Grishin, and T. Okuda, J. Appl. Phys. **88**, 2734 (2000).
[7] S. I. Khartsev and A. M. Grishin, Appl. Phys. Lett. **86**, 141108 (2005).
[8] S. A. Manuilov, R. Fors, S. I. Khartsev, and A. M. Grishin, J. Appl. Phys. **105**, 033917 (2009).

[9]S. A. Manuilov, S. I. Khartsev, and A. M. Grishin, J. Appl. Phys. **106**, 123917 (2009).
[10]SIMNRA official website: www.rzg.mpg.de/~mam/
[11]V. P. Denysenkov and A. M. Grishin, Rev. Sci. Instrum. **74**, 3400 (2003).
[12]H. Suhl, Phys. Rev. **97**, 555 (1955); J. Smit and G. Beljers, Philips Res. Rep. **10**, 113 (1955).
[13]M. Maryško and J. Šimšová, Czech. J. Phys., Sect. B **34**, 1125 (1984).
[14]S. Geller, H. J. Williams, G. P. Espinosa, and R. C. Sherwood, Bell Syst. Tech. J. **43**, 565 (1964).
[15]G. F. Dionne, J. Appl. Phys. **41**, 4874 (1970).
[16]W. P. Wolf, Phys. Rev. **108**, 1152 (1957).
[17]S. Geschwind, Phys. Rev. **121**, 363 (1961).
[18]P. Novák, Czech. J. Phys., Sect. B **34**, 1060 (1984).
[19]H. Callen, Mater. Res. Bull. **6**, 931 (1971).